3D Quantification of Elemental Gradients within Heterostructured Particles of Battery Cathodes

Eva Allen<sup>1,4</sup>, Youngho Shin<sup>3</sup>, William Judge<sup>1,2</sup>, Mark Wolfman<sup>1,6</sup>, Vincent De Andrade<sup>6,7</sup>, Stephanie M. Cologna<sup>1</sup>, Jordi Cabana<sup>1,5\*</sup>

<sup>1</sup>Department of Chemistry, University of Illinois Chicago, Chicago, IL 60608 USA

<sup>2</sup>Element Energy, Inc, Menlo Park, CA 94025 USA

 ${}^3\text{Materials Engineering Research Facility, Applied Materials Division, Argonne National Laboratory, Lemont, IL\,60439,}\\$ 

USA

<sup>4</sup>Applied Materials Division, Argonne National Laboratory, Lemont, IL 60439, USA

<sup>5</sup>Material Science Division, Argonne National Laboratory, Lemont, IL 60439, USA

<sup>6</sup>Advanced Photon Source, Argonne National Laboratory, Lemont, IL 60439, USA

<sup>7</sup>KLA, Milpitas, CA 95035 USA

\*Corresponding Author Email: Jcabana@uic.edu

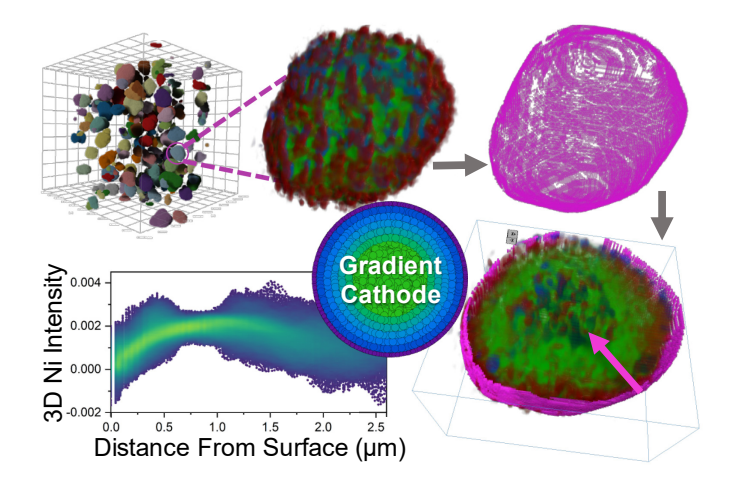
Abstract:

Heterogenous architectures with elemental gradients tailored within particles have been pursued to combat the instabilities limiting Ni-rich cathode materials for lithium-ion batteries. The growth of different compositional layers is accomplished during the synthesis of hydroxide precursors. However, the extent to which these concentration gradients are modified during high-temperature reactions is difficult to establish in their intact, spherical form. Here, we show the entire three-dimensional structure of a secondary particle can be resolved non-destructively with differential X-ray absorption spectroscopy (XAS) through transmission X-ray microscopy (TXM). The relationship between particle location and elemental content was fully quantified, with high statistical significance, for heterostructures possessing different compositional gradients in the precursors with 90:5:5 Ni:Mn:Co core compositions. Reduced

elemental heterogeneity was observed after high-temperature synthesis, but gradients remained. The

methodology presented should be used to guide synthesis while assuring that gains in electrochemical performance are linked to precise elemental distributions at the nanoscale.

### **Table of Contents Figure:**



Lithium-ion batteries have become the leading technology to make the worldwide adoption of electric vehicles (EVs) realized due to their high voltage, high energy density, and long cycle life. To attain further gains in energy density, Ni-rich, Li[Ni<sub>1-x</sub>TM<sub>x</sub>]O<sub>2</sub> (TM = transition metal,  $x \le 0.2$ ), cathode materials have been developed. Li[Ni<sub>0.8</sub>Co<sub>0.15</sub>Al<sub>0.05</sub>]O<sub>2</sub> (LiNCA) and Li[Ni<sub>0.8</sub>Co<sub>0.1</sub>Mn<sub>0.1</sub>]O<sub>2</sub> (LiNMC811) offer a high reversible capacity around 200 mAh g<sup>-1</sup> at relatively low cost. Unfortunately, these cathode compositions suffer from poor thermal stability from oxygen release at highly delithiated states. <sup>2-4</sup> Oxygen release at the cathode surface form impeding surface layers, inhibiting Li-ion diffusion, which is further aggravated by microcrack evolution. <sup>5-7</sup> Insufficient thermal stability leads to safety concerns such as runaway events, which can cause battery pack fires. <sup>8</sup> Therefore, new synthetic strategies to increase the stability of Ni-rich cathodes are urgent for large-scale applications of energy-dense Li-ion cathode materials.

Heterostructured cathode materials have been developed to mitigate degradation. The most common approach are core-shell arrangements, where the core phase provides high energy storage and is protected by a thin shell of a different material to stabilize it against its environment. Classic examples include Albased coatings on various LiNMC compositions. However, the sophistication of cathode heterostructures has grown exponentially in the past decade. One widespread approach driving the design of heterostructures targets a reduction of the interfacial strain when the core and shell have significant epitaxial mismatches through smooth compositional gradients introduced during the growth of the mixed metal precursors. The pinnacle of this approach are materials with a full concentration gradient, where, for instance, the precursors are designed with a linearly decreasing Ni and increasing Mn concentration toward the secondary particle surface. In this case, the increase in Mn confers thermal stability while the smooth transition between different NMC compositions enhances structural stability.

Researchers have honed the ability to fine-tune these materials comprising different compositional layers during precursor synthesis with high accuracy and precision. <sup>22,23</sup> To bring the synthesis of such refined cathodes to manufacturing scales, Shin et al. recently developed a "digital-gradient" process for precursors where a continuous-flow method through cascading continuous stirred tank reactors (CSTR) enabled increasingly complex compositional changes as additional layers on a baseline material. <sup>24</sup> The structures of representative multi-shell architectures made by this method are outlined in Figure 1. Starting from an initial baseline material, Ni<sub>0.9</sub>Co<sub>0.05</sub>Mn<sub>0.05</sub>(OH)<sub>2</sub>, the process was extended to grow a series of additional layers of hydroxide where the Ni:Co:Mn ratios of the synthesis feeds successively changed to 8:1:1, 6:2:2 and 1:1:1, targeting materials with increasing average Mn/Co ratios and compositional differences between interior and surface.

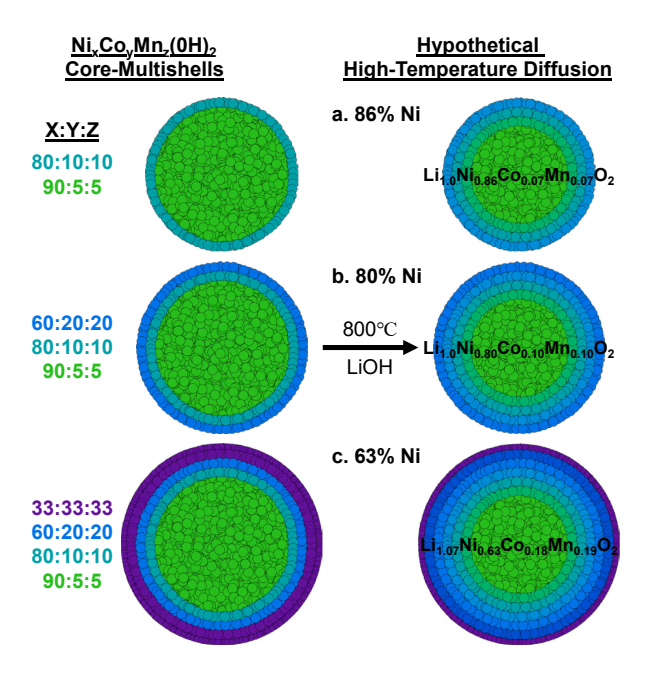


Figure 1. Schematic representation of the cross-sections of the three gradient particle architectures studied in this work. The left column represents the targeted compositional gradients in the hydroxide precursor, with the solution ratios used to grow each compositional layer shown to the left of each particle. The right column represents the hypothesis that annealing at high temperatures to introduce lithium and form the final oxide will induce transition metal interdiffusion in 3D, which motivates our study. The elemental ratios overlaid on each particle correspond to the average elemental composition of the final oxide, measured by ICP.

After these architectures are formed, the precursor is mixed with a lithium salt and sintered at high temperatures (>700°C) to produce the oxide cathode. The elevated temperature causes significant morphological changes, like decreased particle size from dehydration<sup>25</sup> and increased porosity from gas release.<sup>26</sup> More importantly, in the context of the design of heterostructures, it also causes cation interdiffusion of transition metals within secondary particles when compositional gradients exist, <sup>14–18,27,28</sup> changing the elemental profile (Figure 1) and challenging the control of the final architecture. A study was conducted using SEM-EDS measuring linear diffusion coefficients of Ni<sup>3+</sup>, Mn<sup>3+</sup>, and Co<sup>3+</sup> for increasing temperatures performed on laminar pressed pellets, due to the difficulty of measuring

concentration profiles in the radial direction, which found that Co<sup>3+</sup> exhibited a 10x higher diffusion rate than Mn<sup>3+</sup> when diffusing opposite Ni<sup>3+</sup>.<sup>29</sup> Insufficient quantification of the actual gradients in their final form, and their homogeneity across the particle morphology, introduces the risk of misinformed assignment of performance gains and misdirection of future synthesis.

Conventionally, elemental gradients are quantified using SEM-EDS line (i.e., 1D) scans across cross-sections of particles, prepared by mechanical cross-sectioning.<sup>27</sup> Running a 1D scan along a single plane can introduce bias and uncertainty, especially when the depth of probing of EDS is considered. Furthermore, statistical significance is low with such small data sets. Complementary qualitative information is often acquired with elemental (color) maps in 2D, but quantification demands long measurement times that are rarely pursued. Lastly, determination of the location of the measured cross-section within the original secondary particle demands additional particle size measurements. Ultimately, the homogeneity of elemental gradients in secondary particles cannot be confidently established without quantifying the entire 3D volume. FIB-SEM can be used for this purpose but still requires slow, mechanical techniques that may damage the internal morphology and induce redistribution of fragments that introduce uncertainty.

Alternatively, full-field transmission X-ray microscopy (TXM) is a non-destructive technique that can resolve the entire 3D volume via tomography by collecting and reconstructing X-ray projection images across 180°. With synchrotron light sources, the energy of the incident X-rays can be tuned over a wide range. For different elements, the absorption coefficient undergoes step changes at their characteristic absorption edges, compared to smooth changes at all other energies.<sup>30</sup> The sample absorption intensity is proportional to concentration.<sup>31</sup> Relative elemental specificity can be obtained through the difference between the edge-jumps from above and below each K-edge of interest.<sup>30,32–35</sup>

Here, dual-energy TXM was collected at each elemental K-edge to map Ni, Mn, and Co in secondary particles of the three compositional gradient architectures synthesized by Shin et al., outlined in Figure 1.<sup>24</sup> A high statistical significance of the radial concentration profiles in secondary particles was attained for the first time, indicating that diffusion significantly evens out, but does not completely eliminate, the initial compositional gradients towards the average composition of the material. Reduced heterogeneity of elemental content was observed to a greater extent for Ni and Co compared to Mn and in cathode particles with more compositional layers synthesized in the precursor. This method can easily be scaled for the automatic measurement of more particles to acquire further insight into the consistency of interparticle gradients. The methodology provides a feedback loop to build comprehensive theories of cation interdiffusion in heterostructures, informing the design of tailored heterostructured cathodes for Li-ion batteries with high energy density and durability.

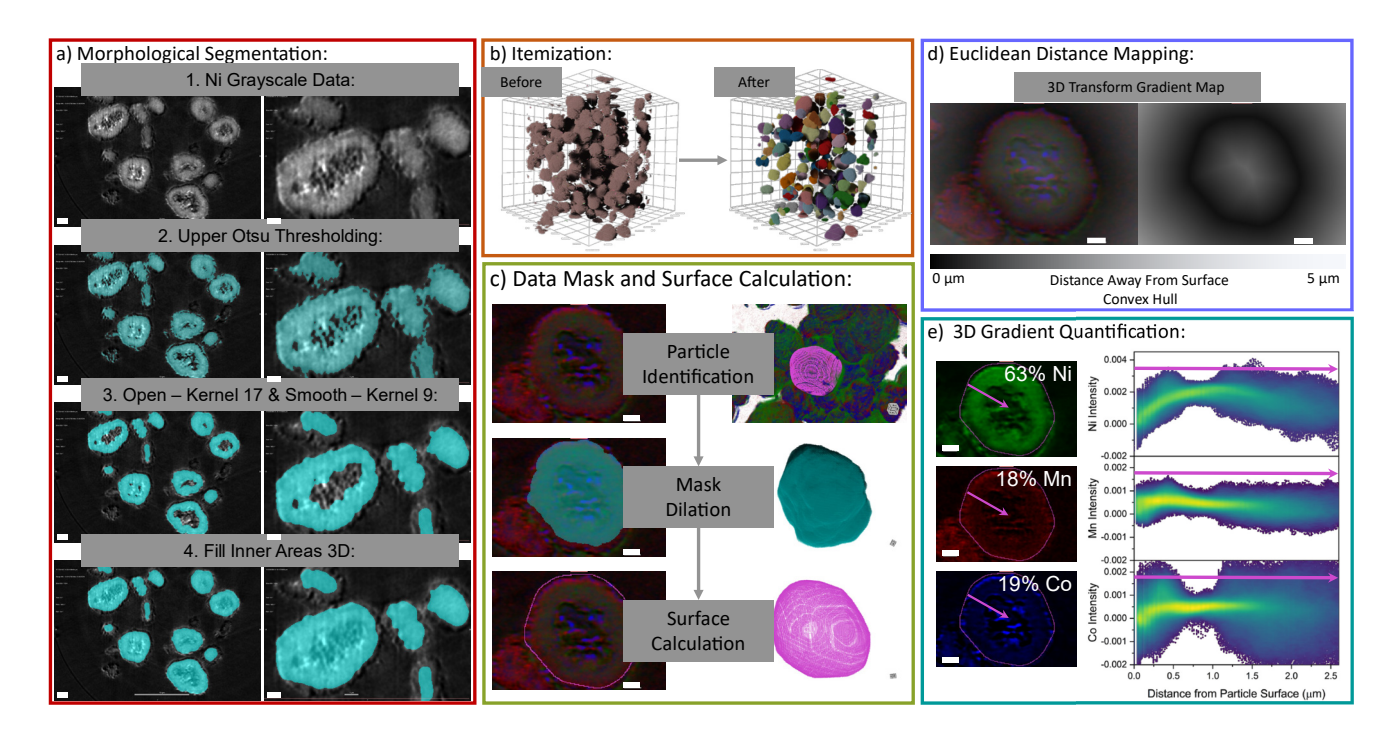


Figure 2. The workflow for the quantification of elemental gradients in three-dimensions. a) Morphological segmentation based on the Ni tomography data. b) Itemization before and after morphological segmentation, showing improved particle separation. c) Dilation of data mask to cover

Mn and Co data and convex hull surface calculation. d) Euclidean distance transform calculated from the surface convex hull. e) The mean elemental percentages for the sampled volume are overlaid on the cross-sectional slices (left). The intensity for each element is plotted (right) for all the mapping positions at the same distance from the particle surface (see pink arrow in both image and graph). The color indicates the density of mapping positions with the same value of intensity, from highest in yellow, to lowest in purple. All scale bars are 1  $\mu$ m.

After the collection of dual-energy TXM of the three gradient architectures in Figure 1, the two-dimensional projection files for the energy pairs were aligned as described in the SI and shown in Figure S1. The data was reconstructed, and the elemental sets were aligned in three dimensions. The workflow outlined in Figure 2 was developed to fully quantify the concentration profiles of TMs after the formation of the lithium transition metal oxide. The particles were first binarized and separated for each field of view through segmentation transforms based on morphological features (Figure 2a-c). The resulting location of the particle surface was used to determine Ni, Co, and Mn profiles as a function of depth. For this purpose, Euclidean Distance Mapping (EDM) transformed the calculated particle surface into an intensity gradient map with normalized pixel intensity equal to increasing distance (Figure 2d). EDM allowed the visualization of the 3D spatial dependence of elemental gradients. Statistical significance of the elemental distribution at each distance point was obtained from the data density plots in Figure 2e, representing the concentration of each element versus particle depth.

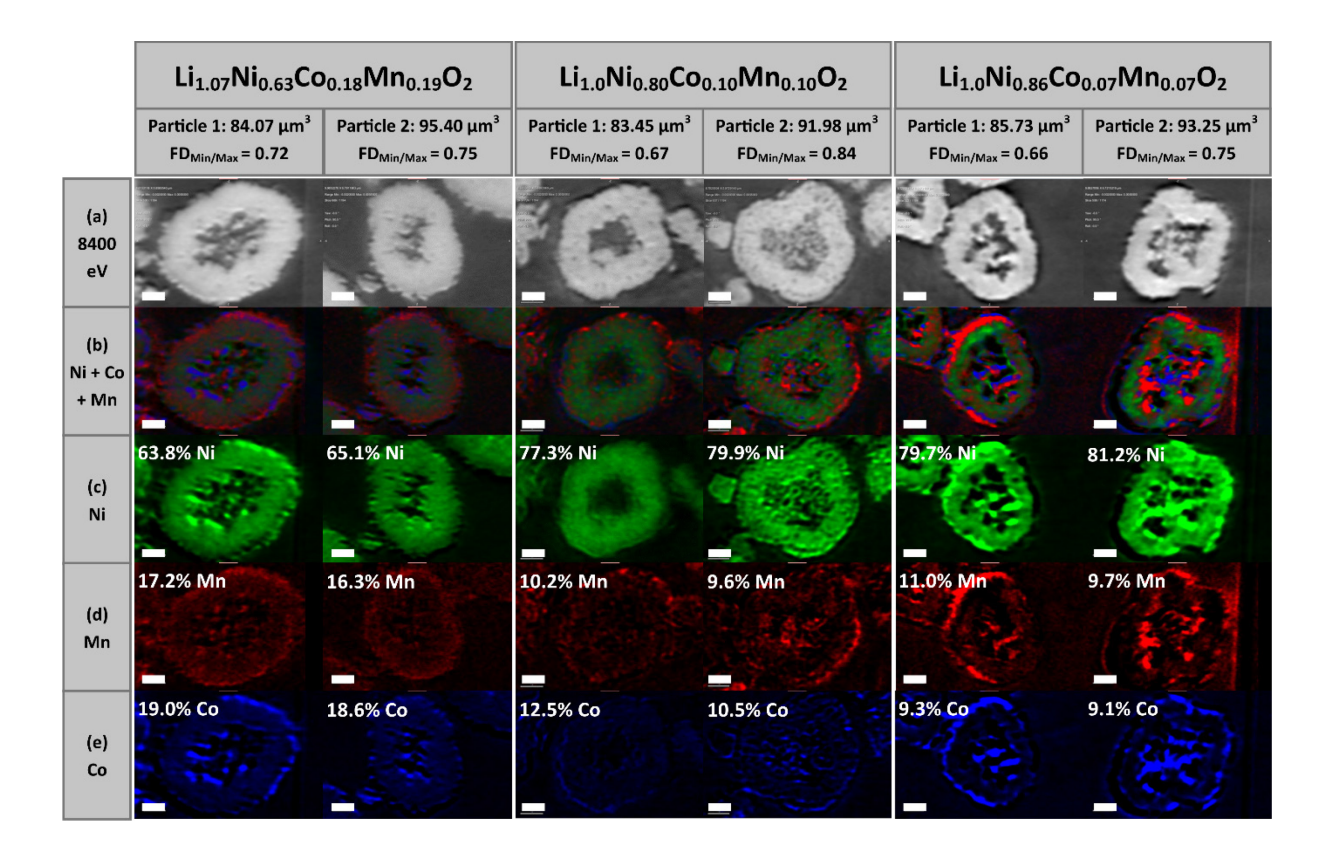


Figure 3 Six particles were sampled from the differential absorption tomography dataset spanning three different gradient compositions. The average elemental percentages are calculated from the mean intensity of the sampled particle volumes. The average composition of the samples measured by ICP are indicated in the top row of each column: Li<sub>1.07</sub>Ni<sub>0.63</sub>Co<sub>0.18</sub>Mn<sub>0.19</sub>O<sub>2</sub>, Li<sub>1.0</sub>Ni<sub>0.80</sub>Co<sub>0.10</sub>Mn<sub>0.10</sub>O<sub>2</sub>, and Li<sub>1.0</sub>Ni<sub>0.86</sub>Co<sub>0.07</sub>Mn<sub>0.07</sub>O<sub>2</sub>. Images in row (a) were collected at 8400 eV, whereas the maps in (b) superimpose the distribution of elemental intensities, and (c-e) are maps of the intensities of the individual element. All scale bars are 1 μm.

The dual-energy TXM collected for the three gradient architectures are shown in Figure 3. The particles were fairly spherical, according to assessments of FD $_{\perp min/max}$ , the quotient between the minimum diameter of the particle and the maximum orthogonal value. In general, the particles showed values spanning 0.66-0.75, with 1 representing the perfectly spherical limit. Two particles of different volumes (84±1  $\mu m^3$  and 94±2  $\mu m^3$ ) were chosen in each gradient architecture for further analysis. Comparisons of representative slices of the particles at 8400 eV are shown in Figure 3, extracted after tomographic reconstruction. The

thickness of each data slice that made up the total TXM volume is equal to the ~0.049-micron pixel spacing, removing projection effects in the raw 2D image as collected. Thus, these thin slices provide enhanced quality of visualization of particle morphology and internal porosity compared to cross-sectional SEM. The differential absorption of the K-edge energy pairs produced maps of elemental intensity (colored maps in Figure 3). Average elemental percentages for each particle were calculated based on the total Ni, Mn, and Co intensity values collected over their entire volume (Figure 2). These values were in high agreement with previous elemental analysis, <sup>24</sup> which verifies the elemental specificity of the differential absorption technique. There was a greater deviation between average differential absorption percentages and reported values for the 86%Ni sample, ~5% vs. ~2% or less in the other two samples.

# Cross-sectional Line Scans of Elemental Specific Tomography: 63% Ni

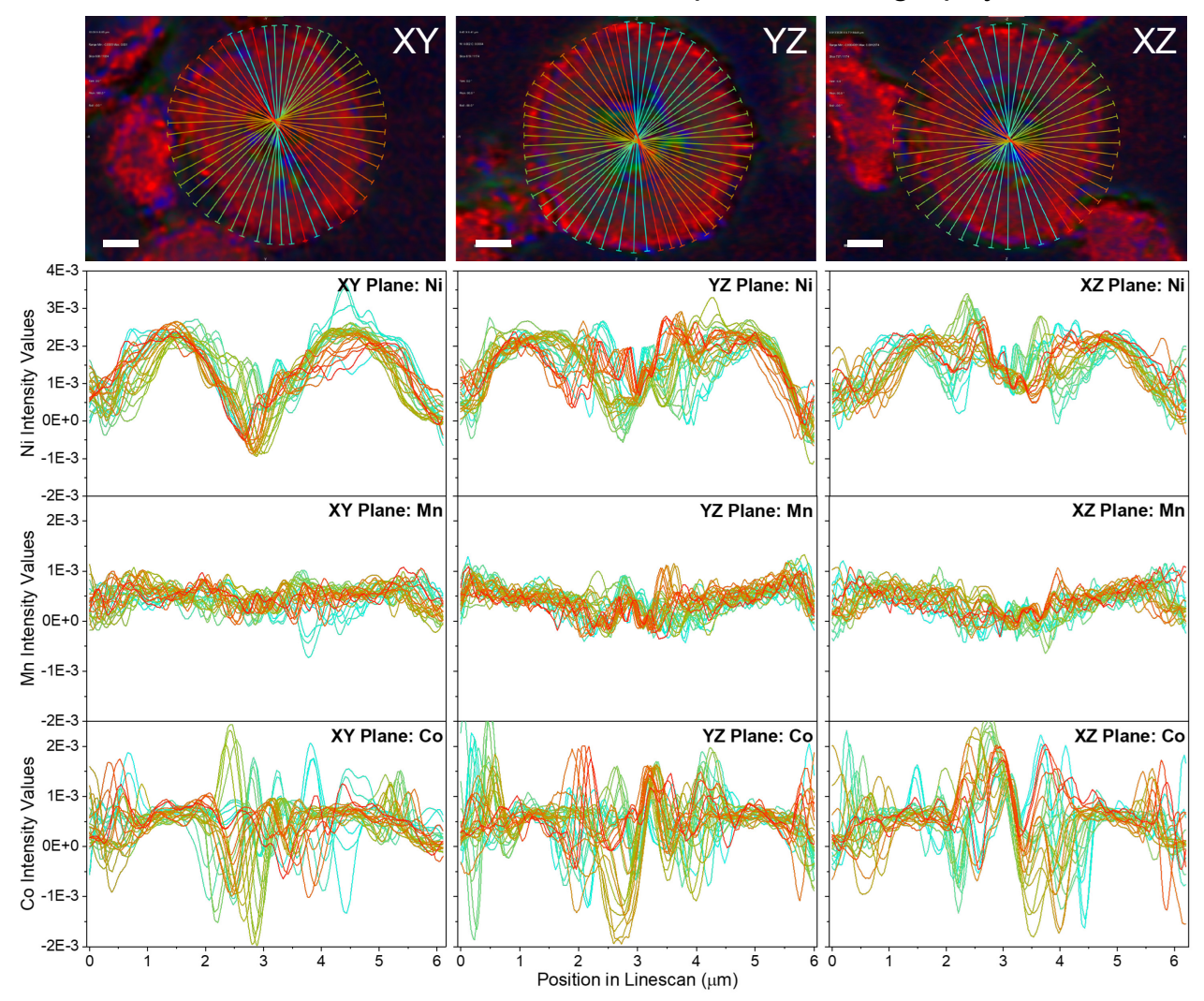


Figure 4. Elemental linescans sampled from the TXM data. Linescans were collected radially through three imaging planes from the center of a single particle of the 63%Ni sample. Scale bars are 1  $\mu$ m. The plots show the positional dependence of the elemental intensities. The linescan color indicates the radial position in the images.

Limitations in the characterization of concentration gradients in a heterostructure arise from simplifying a three-dimensional object to a one-dimensional measurement through linescans of a single viewing plane. To avoid this pitfall, we started our analysis with a series of elemental linescans that were measured radially and superimposed across three orthogonal slices of the tomogram of a 63%Ni particle (Figure 4.).

Its precursor was grown with four different compositional feeds (Figure 1c),<sup>24</sup> naturally giving it the largest compositional variation between surface and center. The Ni and Mn linescans showed systematic and rather reproducible intensity gradients within the three planes. For Mn, the gradient was indicated by an increase in intensity at either end of the linescans, i.e., from the particle center to either surface. The intensity increase appeared more evident in the YZ and XZ planes than in XY, hinting at heterogeneity within the 3D volume. Comparatively clearer evidence of 3D heterogeneity was seen for Ni. Stark differences in intensity profiles were seen between all three planes, especially in the particle center, where the most extensive porosity was observed, particularly in the XY plane. Generally, the Ni intensity increased on either side of the center, reached a maximum, and then decreased to the edge. Lastly, in contrast to Ni and Mn, the intensity profiles of Co showed notable dispersion between different linescans in the same plane. Interestingly, similar profiles were clustered by radial position (i.e., the same color in Figure 4.), suggesting that perhaps the fluctuations could be arising from heterogeneity in the Co distribution. Despite the existence of trends that appeared systematic, these observations were vulnerable to noise, which requires the sampling of the entire structure to determine which trends were statistically significant.

The trends of individual linescans were sufficiently consistent in the 3D volume to make further analysis of compositional gradients reliable. To this end, statistical significance was pursued by classifying data points according to their distance from the center of each particle using EDM (Figure 2d). This choice was motivated by the hypothesis that, during synthesis, gradients are introduced as the particle grows, i.e., new compositional layers are added increasingly away from the center. Drops in the total intensity occur when material is absent, such as at the edge of the particles and in the voids that were common in the center of the secondary particles across all compositions (Figure 3). The low total intensity in these regions could artificially skew the quantification of elements. Overall, evaluations of the total intensity as a

function of incoming energy and relative position in the particle (Figure S2) revealed that the sampling region with the highest confidence was between  $\sim 0.25 \ \mu m$  to  $\sim 2.0 \ \mu m$  from the particle surface. The most considerable drop in total intensity due to the existence of voids in the center was in the last 10-15% of the segmented data for all particles.

The workflow in Figure 2 creates the automatic and objective evaluation of the elemental composition with standardized starting points based on surface morphology. Figure S3 presents the distribution of values of intensity of each element, extracted from the quantification above and below each K-edge, as a function of distance from the center. Figure S2b collapses this graph of data distribution into a mean with an interval of 99% confidence to avoid confusion by the outliers, especially negative values of intensity that have no physical meaning. The segmentation grouped enough data points into a single metric (distance from the center) to produce a value of intensity with very high statistical confidence, producing intervals that are small enough at some distances not to be visible in the plot.

The elemental ratios were subsequently calculated from the plots in Figure S2b using the following equation

Elemental Ratio = 
$$\frac{\text{Elem.}_{\text{int}}}{\text{Ni}_{\text{int}} + \text{Mn}_{\text{int}} + \text{Co}_{\text{int}}}$$
(1)

Where the intensity associated with the K-edge of each element, Elem<sub>int</sub>, was divided by the sum of the three elemental intensities at each position. This approach cancels out the effect of mass on the observed intensity for each element. The values ≤0 in Figure 5, carried over from the density plots in Figure S3, were due to phase artifacts in regions with no material translating into negative values after the difference calculation. Elemental ratios above one and below zero (see Ni and Co at 1.25-1.5 mm into particle 1 of 86%Ni, Figure 5) are left in the plots for transparency, but they should not be regarded as actual elemental

content and are best approximated to 1 and 0, respectively. We note that these outliers are found in the regions of the crystal outside of the domains of highest confidence defined above and in the SI.

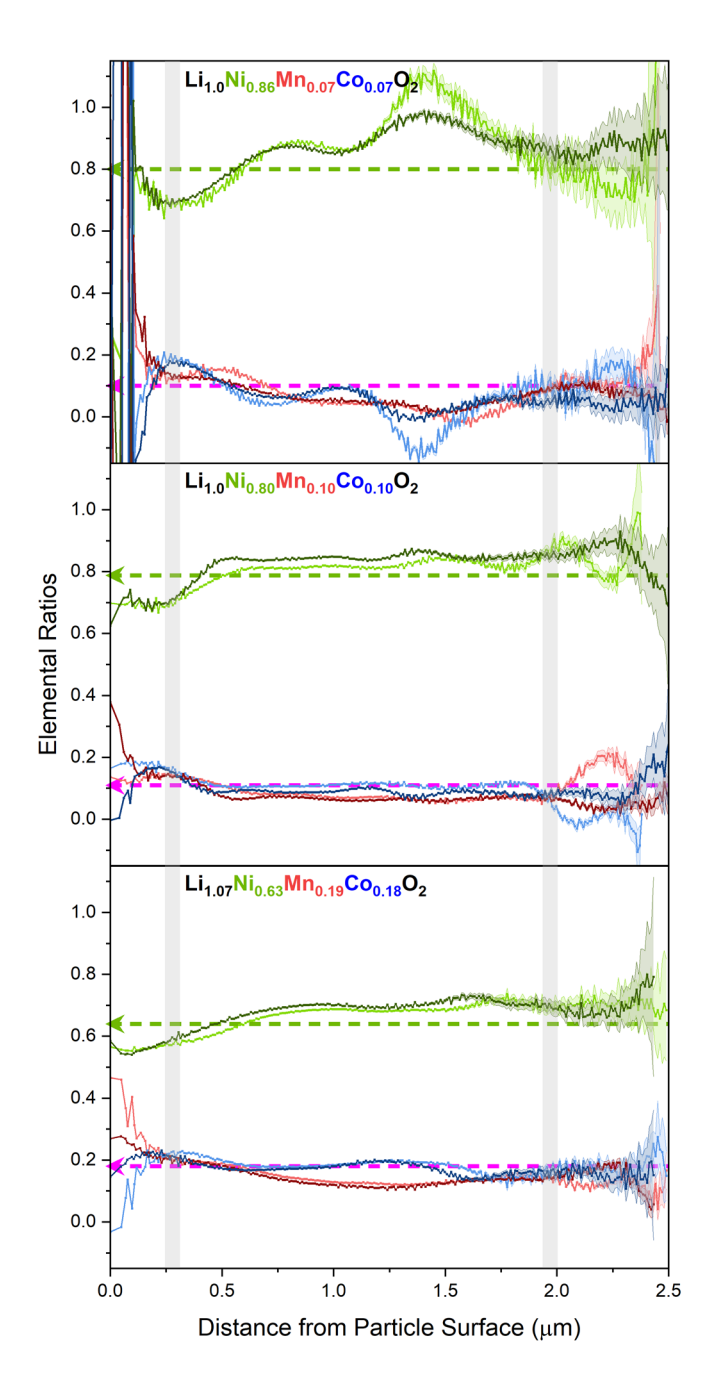


Figure 5. The calculated elemental ratios from the elemental intensity graphs shown in S2b. The error bars indicate the calculated 99% confidence interval for all plots. The two particles used in these plots are shown in Figure 4. The comparison region for the concentration gradients are indicated with the vertical grey lines at the surface, 0.25, and internal porous region, 2.0 μm. The total elemental ratio means reported in Figure 3 are plotted as horizontal dashed lines for Ni (green) and combined Mn and Co (pink).

Table 1: Selection of elemental ratios sampled from representative points in Figure 5.

Gradient Architecture	Element	Particle Number	Near Particle Edge (0.25 - 0.30 μm)		Near Particle Core (1.95 - 2.00 μm)		*D/E1 1	Highest Value (0.25 - 2.00 μm)		¥D (El
			Distance Point /µm	Elemental Ratio (99% CI)	Distance Point /µm	Elemental Ratio (99% CI)	*D(Elemental Ratio) <sub>core-edge</sub>	Distance Point /µm	Elemental Ratio (99% CI)	- <sup>¥</sup> D(Elemental Ratio) <sub>max-min</sub>
2	0.27	0.682(0.005)	2.00	0.88(0.04)	0.19	1.41	0.986(0.009)	0.305		
Mn	1	0.30	0.1296(0.0004)	1.95	0.085(0.006)	-0.044	0.42	0.1677(0.0005)	0.198	
	2	0.26	0.1420(0.0004)	1.95	0.081(0.006)	-0.061	0.26	0.1420(0.0004)	0.1302	
Co	1	0.27	0.2021(0.0009)	1.95	0.06(0.02)	-0.15	0.25	0.208(0.002)	0.352	
	2	0.27	0.1799(0.0009)	2.00	0.03(0.02)	-0.15	0.27	0.1799(0.0009)	0.1941	
80%Ni	Ni	1	0.25	0.6906(0.0006)	1.99	0.90(0.02)	0.21	1.99	0.90(0.02)	0.22
		2	0.26	0.6951(0.0009)	1.98	0.86(0.02)	0.17	1.35	0.874(0.003)	0.179
	Mn	1	0.26	0.1468(0.0005)	1.99	0.062(0.006)	-0.085	0.26	0.1468(0.0005)	0.0967
		2	0.26	0.1456(0.0009)	1.98	0.059(0.004)	-0.087	0.33	0.1460(0.0003)	0.0927
	Co	1	0.28	0.1679(0.0004)	2.00	0.022(0.008)	-0.146	0.28	0.1679(0.0004)	0.1462
		2	0.25	0.161(0.001)	1.99	0.07(0.01)	-0.09	0.25	0.1610(0.001)	0.1000
63%Ni	Ni	1	0.26	0.5713(0.0005)	1.99	0.71(0.03)	0.14	1.78	0.74(0.02)	0.16
		2	0.25	0.5788(0.0005)	1.98	0.70(0.02)	0.13	1.57	0.733(0.008)	0.154
	Mn	1	0.26	0.2079(0.0002)	1.98	0.129(0.005)	-0.079	0.26	0.2079(0.0002)	0.089
		2	0.27	0.2124(0.0004)	1.97	0.140(0.005)	-0.072	0.27	0.2124(0.0004)	0.1084
	Co	1	0.28	0.2280(0.0005)	1.99	0.15(0.02)	-0.08	0.32	0.2293(0.0005)	0.1166
		2	0.25	0.2154(0.0004)	1.97	0.14(0.01)	-0.07	0.25	0.2154(0.0002)	0.0828

<sup>\*</sup>D(Elemental Ratio)<sub>core-edge</sub>: Measurement of the difference in elemental content at core and edge positions

The composition profiles of the three architectures in Figure 5 confirm the existence of concentration gradients in the final layered oxide. There were significant increases in Ni content and corresponding decreases in Mn and Co content between 0.25 and 0.6-0.7 µm from the particle surface across all architectures. In this region, the Ni ratios changed from being lower than the average elemental content measured in the corresponding particle (Figure 3) for the whole sample by Shin et al.,<sup>24</sup> to being higher

<sup>¥</sup>D(Elemental Ratio) max-min: Measurement of the difference in elemental content at absolute max and min between the sampling region (0.25 - 2.00 μm)

closer to the particle center (Figure 5 and Table 1). The opposite trend was observed for Co and, especially, Mn. The compositional profiles oscillated below the ensemble average beyond 0.6-0.7 µm from the particle surface toward the center. Distinct shape differences in the elemental profiles occurred, with oscillations increasing in magnitude from 63%Ni to 86%Ni. When comparing the elemental intensity signals in Figure S2b to the elemental ratios in Figure 5, it was clear that oscillation occurred in all signals, but seemingly to a greater extent for Co. It is interesting to note that the two particles measured showed qualitatively similar oscillations in elemental ratios, suggesting a remarkable consistency between particles is possible with these synthetic methods.

The high confidence of the values measured allowed quantification of gradients. We first compared values around 0.25 and 2.0 μm, D(Elemental Ratio)<sub>core-edge</sub> in Table 1, where values were reasonably stable and not subject to oscillations. The decrease in Ni ratio was 0.14/0.13 for 63%Ni (Table 1, Particle 1/Particle 2), while greater decreases of 0.21/0.17 and 0.18/0.19 were observed for 80%Ni and 86%Ni, respectively. The gradient in Co ratio was also lower for 63%Ni (increase of 0.08/0.07 from core to surface) compared to 80%Ni (0.15/0.09) and 86%Ni (0.15/0.15). In contrast, the extent of increase in Mn ratio from core to surface did not show a clear trend across the samples, with 0.079/0.072 for 63%Ni, 0.085/0.087 for 80%Ni, and 0.044/0.061 for 86%Ni. In previous studies, higher linear interdiffusion rates were measured for Ni and Co compared to Mn,<sup>29</sup> which could account for the greater decrease in heterogeneity of elemental content for those elements at longer spatial distances.

To assess the extent of oscillations in composition, Table 1 also reports the difference between maximum and minimum values observed for each sample between 0.25 μm and 2.0 μm, D(Elemental Ratio)<sub>max-min</sub>. For 86%Ni, the D(Elemental Ratio)<sub>max-min</sub> for Ni was 0.48/0.305, for Mn 0.198/0.130, and Co 0.352/0.194. These values of D(Elemental Ratio)<sub>max-min</sub> were up to four times greater than D(Elemental Ratio)<sub>core-edge</sub>, reflecting a large oscillation between surface and core. For 63%Ni and 80%Ni, the range of values of

D(Elemental Ratio)<sub>max-min</sub> were closer to D(Elemental Ratio)<sub>core-edge</sub> reflecting smaller oscillations in composition from surface to core than 86%Ni. The reduced oscillations in concentration could indicate that additional compositional layers in the precursor state led to more even elemental diffusion during lithiation aided by the greater distance between surface to core composition.

Since the mass of the material notably decreased outside of the range between 0.25 and 2.0 µm from the particle surface (Figure S2a), smaller sampling sizes existed at those distances. Going back to Figure 5, beyond 2.0 µm, the lower sampling sizes induced by particle voids significantly widened the intervals of composition at 99% confidence, making the assessment of gradients unreliable. However, these intervals remained rather narrow between 0 and 0.25 µm. It is intriguing that compositional gradients were apparent at such narrow spatial distances. Specifically, there was a systematic trend for Mn enrichment at the expense of Co in all three samples. The Ni ratio remained comparably stable in 63%Ni and 80%Ni, but there was a visible enrichment in 86%Ni, further adding to the spatial variability of composition for this latter material. Further exploration of variations at such short distances demands techniques with higher spatial resolution, like transmission electron microscopy. The analysis method can be easily applied to complementary techniques such as X-ray fluorescence tomography to attain higher elemental sensitivity at the sacrifice of reduced penetrative power compared to TXM. Evidence has been found that Ni oxidation state may trend with decreasing elemental content from Ni<sup>3+</sup>to Ni<sup>2+</sup>from core to surface using 2D X-ray absorption near-edge structure (2D-XANES) mapping<sup>36</sup>. With the collection of XANES tomography, the trend can be confirmed with statistical significance.

Analysis of TM distribution in gradient architectures after high-temperature sintering is an elusive task when limited to a two-dimensional plane. Through a completely non-destructive TXM differential absorption tomography technique, Ni, Co, and Mn relative elemental ratios were attained across the entire three-dimensional structure spanning many particles from a synthetic batch. The presented study outlines

a methodology to determine the statistical significance of depth-dependent elemental architectures in secondary cathode particles. The gradient architectures were fully quantified using morphological-based segmentation and Euclidean Distance Mapping. There was high elemental homogeneity between two particles across the three architectures. Statistically significant elemental gradients were present in all architectures. While the hydroxide precursors were designed by adding compositional layers to the same core, Ni<sub>0.9</sub>Co<sub>0.05</sub>Mn<sub>0.05</sub>(OH)<sub>2</sub>, TM migration took place during the treatment at high temperature to form the final oxide, evening out the initial compositional gradients toward the average concentration in the particles. There was an apparent correlation between the extent of migration through the secondary particle and the number of initial compositional layers. Since gradients clearly remained after the synthesis, it is possible that further systematic studies could quantify rules of design by manipulating temperatures of synthesis, which, in turn, may help guide future precursor synthetic targets. The methodology established to characterize the elemental gradient architectures was agnostic to composition and should be considered a critical assessment tool when pursuing cathode heterostructures with varying elemental content at the lab-bench to pre-pilot scale.

#### **Acknowledgements:**

This work was primarily supported by the National Science Foundation, under Award CBET-2022723. This research used beamline 32-ID-C of the Advanced Photon Source, a US Department of Energy (DOE) Office of Science User Facility operated for the D.O.E. Office of Science by Argonne National Laboratory under Contract No. DE-AC02-06CH11357.

We gratefully acknowledge the support of the U.S. Department of Energy, Office of Energy Efficiency and Renewable Energy, Vehicle Technologies Office, under Contract No. DE-SC0012704, and in particular the support of Peter Faguy and Dave Howell. This work was partially carried out at the MERF

facility at Argonne National Laboratory, which is supported within the core funding of the Applied Battery Research for Transportation Program. The submitted manuscript has been created by UChicago Argonne, LLC, Operator of Argonne National Laboratory ("Argonne"). The U.S. Government retains for itself, and others acting on its behalf, a paid-up nonexclusive, irrevocable, worldwide license in said article to reproduce, prepare derivative works, distribute copies to the public, and perform publicly and display publicly, by or on behalf of the government.

## **Supporting Information Available:**

Experimental details, a figure depicting data alignment, and preliminary graphs of three-dimensional intensity distribution as a function of distance.

#### **References:**

- (1) Dogan, F.; Vaughey, J. T.; Iddir, H.; Key, B. Direct Observation of Lattice Aluminum Environments in Li Ion Cathodes LiNi<sub>1-y-z</sub>Co<sub>y</sub>Al<sub>z</sub>O<sub>2</sub> and Al-Doped LiNi<sub>x</sub>Mn<sub>y</sub>Co<sub>z</sub>O<sub>2</sub> via 27Al MAS NMR Spectroscopy. *ACS Appl. Mater. Interfaces* **2016**, 8 (26), 16708–16717. https://doi.org/10.1021/acsami.6b04516.
- (2) Lee, E.; Muhammad, S.; Kim, T.; Kim, H.; Lee, W.; Yoon, W. S. Tracking the Influence of Thermal Expansion and Oxygen Vacancies on the Thermal Stability of Ni-Rich Layered Cathode Materials. *Adv. Sci.* **2020**, *7* (12), 1–12. https://doi.org/10.1002/advs.201902413.
- (3) MacNeil, D. D.; Lu, Z.; Chen, Z.; Dahn, J. R. A Comparison of the Electrode/Electrolyte Reaction at Elevated Temperatures for Various Li-Ion Battery Cathodes. *J. Power Sources* **2002**, *108* (1–2), 8–14. https://doi.org/10.1016/S0378-7753(01)01013-8.
- (4) Bak, S. M.; Nam, K. W.; Chang, W.; Yu, X.; Hu, E.; Hwang, S.; Stach, E. A.; Kim, K. B.; Chung, K. Y.; Yang, X. Q. Correlating Structural Changes and Gas Evolution during the Thermal Decomposition of Charged Li<sub>x</sub>Ni<sub>0.8</sub>Co<sub>0.15</sub>Al<sub>0.05</sub>O<sub>2</sub> Cathode Materials. *Chem. Mater.* 2013, 25 (3), 337–351. https://doi.org/10.1021/cm303096e.
- (5) Ahn, Y. K.; Jo, Y. N.; Cho, W.; Yu, J. S.; Kim, K. J. Mechanism of Capacity Fading in the LiNi<sub>0.8</sub>Co<sub>0.1</sub>Mn<sub>0.1</sub>O<sub>2</sub> Cathode Material for Lithium-Ion Batteries. *Energies* **2019**, *12* (9), 1–10. https://doi.org/10.3390/en12091638.
- (6) Heenan, T. M. M.; Wade, A.; Tan, C.; Parker, J. E.; Matras, D.; Leach, A. S.; Robinson, J. B.; Llewellyn, A.; Dimitrijevic, A.; Jervis, R.; Quinn, P. D.; Brett, D. J. L.; Shearing, P. R. Identifying the Origins of Microstructural Defects Such as Cracking within Ni-Rich NMC811 Cathode

- Particles for Lithium-Ion Batteries. *Adv. Energy Mater.* **2020**, *10* (47), 1614-6832. https://doi.org/10.1002/aenm.202002655.
- (7) Ryu, H. H.; Park, K. J.; Yoon, C. S.; Sun, Y. K. Capacity Fading of Ni-Rich Li[Ni<sub>x</sub>Co<sub>y</sub>Mn<sub>1-x-y</sub>]O<sub>2</sub> ( $0.6 \le x \le 0.95$ ) Cathodes for High-Energy-Density Lithium-Ion Batteries: Bulk or Surface Degradation? *Chem. Mater.* **2018**, 30 (3), 1155–1163. https://doi.org/10.1021/acs.chemmater.7b05269.
- (8) Sun, Y.; Ren, D.; Liu, G.; Mu, D.; Wang, L.; Wu, B.; Liu, J.; Wu, N.; He, X. Correlation between Thermal Stabilities of Nickel-Rich Cathode Materials and Battery Thermal Runaway. *Int. J. Energy Res.* **2021**, *45* (15), 20867–20877. https://doi.org/10.1002/er.7143.
- (9) Zhao, R.; Liang, J.; Huang, J.; Zeng, R.; Zhang, J.; Chen, H.; Shi, G. Improving the Ni-Rich LiNi<sub>0.5</sub>Co<sub>0.2</sub>Mn<sub>0.3</sub>O<sub>2</sub> Cathode Properties at High Operating Voltage by Double Coating Layer of Al<sub>2</sub>O<sub>3</sub> and Al<sub>P</sub>O<sub>4</sub>. *J. Alloys Compd.* **2017**, 724, 1109–1116. https://doi.org/10.1016/j.jallcom.2017.05.331.
- (10) Yan, P.; Zheng, J.; Zhang, X.; Xu, R.; Amine, K.; Xiao, J.; Zhang, J. G.; Wang, C. M. Atomic to Nanoscale Investigation of Functionalities of an Al<sub>2</sub>O<sub>3</sub> Coating Layer on a Cathode for Enhanced Battery Performance. *Chem. Mater.* 2016, 28 (3), 857–863. https://doi.org/10.1021/acs.chemmater.5b04301.
- (11) Wang, J. H.; Wang, Y.; Guo, Y. Z.; Ren, Z. Y.; Liu, C. W. Effect of Heat-Treatment on the Surface Structure and Electrochemical Behavior of AlPO4-Coated LiNi<sub>1/3</sub>Co<sub>1/3</sub>Mn<sub>1/3</sub>O<sub>2</sub> Cathode Materials. *J. Mater. Chem. A* **2013**, *I* (15), 4879–4884. https://doi.org/10.1039/c3ta00064h.
- (12) Du, K.; Xie, H.; Hu, G.; Peng, Z.; Cao, Y.; Yu, F. Enhancing the Thermal and Upper Voltage

- Performance of Ni-Rich Cathode Material by a Homogeneous and Facile Coating Method: Spray-Drying Coating with Nano-Al<sub>2</sub>O<sub>3</sub>. *ACS Appl. Mater. Interfaces* **2016**, *8* (27), 17713–17720. https://doi.org/10.1021/acsami.6b05629.
- (13) Kim, Y. J.; Kim, H.; Kim, B.; Ahn, D.; Lee, J. G.; Kim, T. J.; Son, D.; Cho, J.; Kim, Y. W.; Park, B. Electrochemical Stability of Thin-Film LiCoO<sub>2</sub> Cathodes by Aluminum-Oxide Coating. *Chem. Mater.* **2003**, *15* (7), 1505–1511. https://doi.org/10.1021/cm0201403.
- (14) Sun, Y.-K.; Myung, S.-T.; Kim, M.-H.; Prakash, J.; Amine, K. Synthesis and Characterization of Li[(Ni<sub>0.8</sub>Co<sub>0.1</sub>Mn<sub>0.1</sub>)<sub>0.8</sub>(Ni<sub>0.5</sub>Mn<sub>0.5</sub>)<sub>0.2</sub>]O<sub>2</sub> with a Microscale Core-Shell Structure as the Positive Electrode Material for Lithium Batteries. *J. Am. Chem. Soc.* **2005**, *127* (38), 13411–13418. https://doi.org/10.1021/ja053675g.
- (15) Camardese, J.; Li, J.; Abarbanel, D. W.; Wright, A. T. B.; Dahn, J. R. The Effect of Lithium Content and Core to Shell Ratio on Structure and Electrochemical Performance of Core-Shell Li<sub>(1+x)</sub>[Ni<sub>0.6</sub>Mn<sub>0.4</sub>]<sub>(1-x)</sub>O<sub>2</sub> Li<sub>(1+y)</sub>[Ni<sub>0.2</sub>Mn<sub>0.8</sub>]<sub>(1-y)</sub>O<sub>2</sub> Positive Electrode Materials . *J. Electrochem. Soc.* **2015**, *162* (3), A269–A277. https://doi.org/10.1149/2.0081503jes.
- (16) Yang, X.; Wang, X.; Hu, L.; Zou, G.; Su, S.; Bai, Y.; Shu, H.; Wei, Q.; Hu, B.; Ge, L.; Wang, D.; Liu, L. Layered Li[Ni<sub>0.5</sub>Co<sub>0.2</sub>Mn<sub>0.3</sub>]O<sub>2</sub>-Li<sub>2</sub>MnO<sub>3</sub> Core-Shell Structured Cathode Material with Excellent Stability. *J. Power Sources* **2013**, *242*, 589–596. https://doi.org/10.1016/j.jpowsour.2013.05.139.
- (17) Shi, H.; Wang, X.; Hou, P.; Zhou, E.; Guo, J.; Zhang, J.; Wang, D.; Guo, F.; Song, D.; Shi, X.; Zhang, L. Core-Shell Structured Li[(Ni<sub>0.8</sub>Co<sub>0.1</sub>Mn<sub>0.1</sub>)<sub>0.7</sub>(Ni<sub>0.45</sub>Co<sub>0.1</sub>Mn<sub>0.45</sub>)<sub>0.3</sub>]O<sub>2</sub> Cathode Material for High-Energy Lithium Ion Batteries. *J. Alloys Compd.* **2014**, *587*, 710–716. https://doi.org/10.1016/j.jallcom.2013.10.226.

- (18) Sun, Y.-K.; Lee, B.-R.; Noh, H.-J.; Wu, H.; Myung, S.-T.; Amine, K. A Novel Concentration-Gradient Li[Ni<sub>0.83</sub>Co<sub>0.07</sub>Mn<sub>0.10</sub>]O<sub>2</sub> Cathode Material for High-Energy Lithium-Ion Batteries. *J. Mater. Chem.* **2011**, *21* (27), 10108. https://doi.org/10.1039/c0jm04242k.
- (19) Li, Y.; Xu, R.; Ren, Y.; Lu, J.; Wu, H.; Wang, L.; Miller, D. J.; Sun, Y. K.; Amine, K.; Chen, Z. Synthesis of Full Concentration Gradient Cathode Studied by High Energy X-Ray Diffraction.

  Nano Energy 2016, 19, 522–531. https://doi.org/10.1016/J.NANOEN.2015.07.019.
- (20) Liang, M.; Sun, Y.; Song, D.; Shi, X.; Han, Y.; Zhang, H.; Zhang, L. Superior Electrochemical Performance of Quasi-Concentration-Gradient LiNi<sub>0.8</sub>Co<sub>0.15</sub>Al<sub>0.05</sub>O<sub>2</sub> Cathode Material Synthesized with Multi-Shell Precursor and New Aluminum Source. *Electrochim. Acta* **2019**, *300*, 426–436. https://doi.org/10.1016/j.electacta.2019.01.125.
- (21) Sun, Y. K.; Myung, S. T.; Park, B. C.; Prakash, J.; Belharouak, I.; Amine, K. High-Energy Cathode Material for Long-Life and Safe Lithium Batteries. *Nat. Mater.* **2009**, *8* (4), 320–324. https://doi.org/10.1038/nmat2418.
- (22) Liao, J. Y.; Oh, S. M.; Manthiram, A. Core/Double-Shell Type Gradient Ni-Rich LiNi<sub>0.76</sub>Co<sub>0.10</sub>Mn<sub>0.14</sub>O<sub>2</sub> with High Capacity and Long Cycle Life for Lithium-Ion Batteries. *ACS Appl. Mater. Interfaces* **2016**, *8* (37), 24543–24549. https://doi.org/10.1021/acsami.6b06172.
- (23) Hou, P.; Guo, J.; Song, D.; Zhang, J.; Zhou, E.; Zhang, L. A Novel Double-Shelled LiNi<sub>0.5</sub>Co<sub>0.2</sub>Mn<sub>0.3</sub>O<sub>2</sub> Cathode Material for Li-Ion Batteries. *Chem. Lett.* **2012**, *41* (12), 1712–1714. https://doi.org/10.1246/cl.2012.1712.
- (24) Shin, Y.; Maeng, S.; Chung, Y.; Krumdick, G. K.; Min, S. Core–Multishell-Structured Digital-Gradient Cathode Materials with Enhanced Mechanical and Electrochemical Durability. *Small*

- **2021**, 17 (19), 2100040. https://doi.org/10.1002/sml1.202100040.
- (25) Tang, L.; Cheng, X.; Wu, R.; Cao, T.; Lu, J.; Zhang, Y.; Zhang, Z. Monitoring the Morphology Evolution of LiNi<sub>0.8</sub>Mn<sub>0.1</sub>Co<sub>0.1</sub>O<sub>2</sub> during High-Temperature Solid State Synthesis via in Situ SEM. *J. Energy Chem.* **2022**, *66*, 9–15. https://doi.org/10.1016/j.jechem.2021.07.021.
- (26) Yao, Y.; Liu, H.; Li, G.; Peng, H.; Chen, K. Multi-Shelled Porous LiNi<sub>0.5</sub>Mn<sub>1.5</sub>O<sub>4</sub> Microspheres as a 5 v Cathode Material for Lithium-Ion Batteries. *Mater. Chem. Phys.* **2014**, *143* (2), 867–872. https://doi.org/10.1016/j.matchemphys.2013.10.028.
- (27) Zhang, N.; Zaker, N.; Li, H.; Liu, A.; Inglis, J.; Jing, L.; Li, J.; Li, Y.; Botton, G. A.; Dahn, J. R. Cobalt-Free Nickel-Rich Positive Electrode Materials with a Core-Shell Structure. *Chem. Mater.*2019, 31 (24), 10150–10160. https://doi.org/10.1021/acs.chemmater.9b03515.
- (28) Rathore, D.; Garayt, M.; Liu, Y.; Geng, C.; Johnson, M.; Dahn, J. R.; Yang, C. Preventing Interdiffusion during Synthesis of Ni-Rich Core-Shell Cathode Materials. *ACS Energy Lett.* **2022**, 7 (7), 2189–2195. https://doi.org/10.1021/acsenergylett.2c01009.
- (29) Li, J.; Doig, R.; Camardese, J.; Plucknett, K.; Dahn, J. R. Measurements of Interdiffusion Coefficients of Transition Metals in Layered Li-Ni-Mn-Co Oxide Core-Shell Materials during Sintering. *Chem. Mater.* **2015**, *27* (22), 7765–7773. https://doi.org/10.1021/acs.chemmater.5b03499.
- (30) Liu, Y.; Meirer, F.; Wang, J.; Requena, G.; Williams, P.; Nelson, J.; Mehta, A.; Andrews, J. C.; Pianetta, P. 3D Elemental Sensitive Imaging Using Transmission X-Ray Microscopy. *Anal. Bioanal. Chem.* **2012**, *404* (5), 1297–1301. https://doi.org/10.1007/s00216-012-5818-9.
- (31) Dowd, B. A.; Campbell, G. H.; Marr, R. B.; Nagarkar, V. V.; Tipnis, S. V.; Axe, L.; Siddons, D.

- P. Developments in Synchrotron X-Ray Computed Microtomography at the National Synchrotron Light Source. In *Developments in X-Ray Tomography II*; Bonse, U., Ed.; 1999; Vol. 3772, pp 224–236. https://doi.org/10.1117/12.363725.
- (32) Meirer, F.; Cabana, J.; Liu, Y.; Mehta, A.; Andrews, C.; Andrews, J. C.; Pianetta, P. Three-Dimensional Imaging of Chemical Phase Transformations at the Nanoscale with Full-Field Transmission X-Ray Microscopy. *J. Synchrotron Radiat.* **2011**, *18* (5), 773–781. https://doi.org/10.1107/S0909049511019364.
- (33) Yang, F.; Liu, Y.; Martha, S. K.; Wu, Z.; Andrews, J. C.; Ice, G. E.; Pianetta, P.; Nanda, J. Nanoscale Morphological and Chemical Changes of High Voltage Lithium-Manganese Rich NMC Composite Cathodes with Cycling. *Nano Lett.* 2014, 14 (8), 4334–4341. https://doi.org/10.1021/nl502090z.
- (34) Cats, K. H.; Gonzalez-Jimenez, I. D.; Liu, Y.; Nelson, J.; van Campen, D.; Meirer, F.; Van der Eerden, A. M. J.; de Groot, F. M. F.; Andrews, J. C.; Weckhuysen, B. M. X-Ray Nanoscopy of Cobalt Fischer-Tropsch Catalysts at Work. *Chem. Commun.* **2013**, *49* (41), 4622–4624. https://doi.org/10.1039/c3cc00160a.
- (35) Grew, K. N.; Chu, Y. S.; Yi, J.; Peracchio, A. A.; Izzo, J. R.; Hwu, Y.; De Carlo, F.; Chiu, W. K. S. Nondestructive Nanoscale 3D Elemental Mapping and Analysis of a Solid Oxide Fuel Cell Anode. J. Electrochem. Soc. 2010, 157 (6), B783. https://doi.org/10.1149/1.3355957.
- (36) Lin, R.; Bak, S. M.; Shin, Y.; Zhang, R.; Wang, C.; Kisslinger, K.; Ge, M.; Huang, X.; Shadike, Z.; Pattammattel, A.; Yan, H.; Chu, Y.; Wu, J.; Yang, W.; Whittingham, M. S.; Xin, H. L.; Yang, X. Q. Hierarchical Nickel Valence Gradient Stabilizes High-Nickel Content Layered Cathode Materials. *Nat. Commun.* 2021, 12 (1), 1–10. https://doi.org/10.1038/s41467-021-22635-w.